Journal of Zhejiang University-SCIENCE A (Applied Physics & Engineering)
ISSN 1673-565X (Print); ISSN 1862-1775 (Online)
www.jzus.zju.edu.cn; www.springerlink.com
E-mail: jzus@zju.edu.cn

Static analysis of a stepped main shaft in a mine hoist by means of the modified 1D higher-order theory*

Wen-xiang TENG[1], Zhen-cai ZHU[†‡1,2]

[1]School of Mechanical and Electrical Engineering, China University of Mining and Technology, Xuzhou 221116, China

[2]Jiangsu Key Laboratory of Mine Mechanical and Electrical Equipment, China University of Mining and Technology, Xuzhou 221116, China

[†]E-mail: zhuzhencai@cumt.edu.cn

Received Sept. 22, 2017; Revision accepted Jan. 25, 2018; Crosschecked July 18, 2018

Abstract: The analysis of a stepped main shaft by 1D refined beam theories in cylindrical coordinate system is presented. High-order displacement fields are achieved by employing the Carrera unified formulation (CUF), which takes direct implementation of any-order theory without the requirement of considering special formulations. The classical beam theories can be derived from the formulation as particular cases. The principle of minimum potential energy is used to obtain the governing differential equations and the related boundary conditions in a cylindrical coordinate system. These explicit terms of the stiffness matrices are exhibited and a global stiffness matrix is then obtained by matrix transformation. For the special working condition in a mining hoist and stepped shaft, the resulting global stiffness matrix and the loading vector are modified and applied with the boundary conditions in the static analysis of shaft parts. The accuracy of static analysis based on the refined beam theory is confirmed by comparing ANSYS solid theory and classical beam theories. An experiment for verifying the availability of the modified 1D refined beam model on the surface strain of segment 9 of the main shaft is conducted in a field experiment at Zhaojiazhai Coal Mine, China. Experimental results demonstrate the practicability of the present theory in predicting the strain field on the surface of the stepped main shaft of a mining hoist.

Key words: Carrera unified formulation (CUF); 1D higher-order theory; Finite element method; Strain field; Stepped main shaft; Main hoist

https://doi.org/10.1631/jzus.A1700509 **CLC number:** TD444

1 Introduction

Mine safety has become an urgent problem because thousands of miners die from mining accidents around the world every year. This also causes huge economic losses for the state and enterprises. These accidents have a variety of causes including dust explosions, collapsing of mine stopes, flooding, and general mechanical errors from improperly used or malfunctioning mining equipment or systems (Dhillon, 2010). Therefore, how to indicate the hoisting condition accurately via an easy method is of great importance for mine safety. The main shaft is a mechanical rotating component in the hoisting system, and takes the main load when operating. From the mechanical analysis perspective, the main shaft can be seen as a simple-supported beam in a certain condition. To indicate the hoisting condition, beam theories are applied to achieve a main shaft model. Thus, the main shaft can be analyzed using beam assumptions and a 1D approach. This is more efficient than 2D plate and shell models or 3D solid models (Bathe, 1996) in terms of computational cost. The beam

‡ Corresponding author

* Project supported by the National Basic Research Program (973) of China (No. 2014CB049404), the National Key Research and Development Program (No. 2016YFC0600905), the Program for Changjiang Scholars and Innovative Research Team in University (No. IRT_16R68), and the Priority Academic Program Development of Jiangsu Higher Education Institutions (PAPD), China

ORCID: Wen-xiang TENG, https://orcid.org/0000-0001-6667-6722

models, known as classical theories, are the Euler-Bernoulli beam theory (EBBT) (Euler, 1744) and the Timoshenko beam theory (TBT) (Timoshenko, 1921, 1922) with the associated models being Euler-Bernoulli beam model (EBBM) and Timoshenko beam model (TBM). However, the classical theories have disadvantages. Transverse shear deformation is ignored in the EBBT and a constant shear strain across the section is assumed in the TBT. Given that the main shaft in deep hoisting is composed of several segments of short shafts and taken together with assumptions in classical theories, it is difficult to obtain reliable results of the required accuracy on the surface of segments. Therefore, we need to overcome the problems caused by these assumptions.

A lot of effort has been put in over the years to ameliorate the disadvantages of the beam theories. For example, several refined 1D and 2D theories have been developed. Not only can these theories maintain a simple format and involve low computational cost, but also are able to explore non-classical characteristics to give the required level of accuracy. A review of the most influential approaches to developing beam models with particular emphasis on the Carrera unified formulation (CUF) and its application was presented in (Carrera et al., 2015a). A lot of refined beam theories have been proposed. Their methods (Cowper, 1966; Jensen, 1983; Gruttmann and Wagner, 2001; Hutchinson, 2001; Chan et al., 2011) mainly focus on torsional and flexural shearing stresses in prismatic beams with arbitrary shaped cross-sections to take a suitable shear correction factor into consideration. A new TBM was developed using a modified couple stress theory and a surface elasticity theory by Gao (2015), which considered additional material constants. Stephen and Levinson (1979) proposed a second-order beam theory which takes shear curvature, transverse direct stresses, and rotatory inertia into consideration. The nonlinear phenomenon of axial tension was taken into consideration in the elastic TBT and the corresponding stiffness equations for finite rotation in (Tetsuo, 1990). An overview of various refined shear deformation theories adopted for the analyses of composite beams, with particular emphasis on static behavior, was given in (Vo and Thai, 2012). The stiffness, mass, and consistent force matrices were developed based upon Hamilton's principle for a simple two-node Timoshenko beam element in (Friedman and Kosmatka, 1993).

The beam theories developed are problem dependent in the aforementioned studies, that is, different problems require adaptation for different models. Carrera et al. (2011) and Carrera and Petrolo (2012) proposed the CUF for 1D theories, which is used to formulate variable kinematic 1D elements on the basis of Taylor-type expansion (TE) in the present work. TE models are obtained by utilizing the Taylor-like polynomials of order N to describe the displacement field over the cross-section, in which N is regarded as a free parameter of the CUF. Classical beam theories, such as EBBT and TBT, can be retrieved as special cases from the formulation. Several axiomatic refined theories for the linear static analysis of beams made of isotropic materials were proposed by Carrera and Giunta (2010), where an N-order approximation via MacLaurin's polynomials is assumed on the cross-section for the displacement unknown variables. In (Carrera et al., 2015b), the application of an advanced 1D variable kinematic model to analyze typical civil engineering structures was proposed, whereas Carrera and Petrolo (2011) handled refined beams theories with an increasing number of displacement variables. The investigation of the static and dynamic analysis of solid and thin-walled structures, using the CUF beam theories, was carried out in (Pagani et al., 2013, 2015, 2016; Filippi et al., 2015). These results demonstrated the effectiveness of the CUF beam theories in terms of accuracy and computational efficiency.

In this work, CUF is employed to establish the modified high-order beam theory which is the basis of main shaft modeling. Then a static analysis of the main shaft in a mine hoister is carried out. The results are compared with the commercial finite element method (FEM) code analyses, classical beam models, and experimental results.

2 Classical beam theories

The Cartesian coordinate system shown in Fig. 1 is adopted for a circular shaft. The longitudinal axis of the circular shaft is the coordinate z ($0 \le z \le L$). Although the cross-section Ω shown in Fig. 1 is circular, the effectiveness of the proposed approach does not depend on the shape of the cross-section. Based on the

Cartesian coordinate system, the displacement field of EBBM is

$$\begin{aligned} u_x(x,y,z) &= u_{x1}(z), \\ u_y(x,y,z) &= u_{y1}(z), \\ u_z(x,y,z) &= u_{z1}(z) - x\frac{\partial u_{x1}(z)}{\partial z} + y\frac{\partial u_{y1}(z)}{\partial z}, \end{aligned} \tag{1}$$

where u_x, u_y, and u_z stand for the displacement components of coordinate points belonging to the shaft along x, y, and z axes, respectively; u_{x1}, u_{y1}, and u_{z1} are the displacements of the coordinate axis; the terms $-\frac{\partial u_{x1}(z)}{\partial z}$ and $\frac{\partial u_{y1}(z)}{\partial z}$ describe the rotations of the cross-section about the y axis (i.e. ϕ_y) and x axis (i.e. ϕ_x).

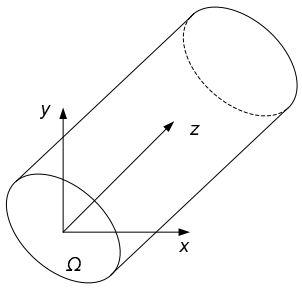

Fig. 1 Cartesian coordinate system of the beam model

As assumed by the EBBT, the distortional cross-section maintains plane and orthogonal to the beam axis since the shear deformation phenomena over cross-section are ignored. Incorrect results are obtained when neglecting the shear stresses in dealing with several problems (e.g. short beams and structures).

To overcome the assumption of the cross-sectional orthogonality in EBBM, the improved displacement field is adopted in TBM:

$$\begin{cases} u_x(x,y,z) = u_{x1}(z), \\ u_y(x,y,z) = u_{y1}(z), \\ u_z(x,y,z) = u_{z1}(z) + x\phi_y(z) - y\phi_x(z). \end{cases} \tag{2}$$

The unknown rotations, ϕ_x and ϕ_y, are added to the formulation. That is, the aforementioned assumptions of the EBBT cannot be taken into consideration, and it is clear that TBT is an improved theory and its application range is expanded.

3 Carrera unified formulation models based on Taylor series in the cylindrical coordinate system

Although the classical beam models can achieve satisfactory results when slender, solid-section, homogeneous structures are subjected to bending loads, several problems (e.g. short beams and assembled shafts undergoing bending and transverse loads) need more sophisticated theories to achieve sufficiently accurate results. The CUF (Carrera et al., 2011) can be used to solve this issue by describing the cross-sectional displacement field via expansions.

According to the CUF, the displacement field of a beam model is expressed as

$$\boldsymbol{u}(x,y,z) = \psi_i(x,y)\boldsymbol{U}_i(z), \quad i = 1,2,\cdots,n, \tag{3}$$

where $\boldsymbol{u}(x, y, z)=[u_x(x, y, z), u_y(x, y, z), u_z(x, y, z)]^{\mathrm{T}}$ is the transposed displacement vector in the Cartesian coordinate system; ψ_i denotes the expansion functions on the cross-section; $\boldsymbol{U}_i$ is a function matrix of axial displacement extension and n indicates the number of terms in the expansion. The subscript "i" indicates summation because of the adoption of the generalized Einstein notation. The class of the 1D model is determined by the choice of ψ_i varying over the cross-section, whereas the choices and n are arbitrary. In this study, the expansion functions ψ_i shown in Table 1 are written as MacLaurin's polynomials. This approach was adopted to establish the model of the stepped main shaft in a mine hoister. For this reason, this class of models is named the TE model. EBBM and TBM are special cases of the linear (N=1) TE model, which can be written as

$$\begin{cases} u_x = U_1 + xU_2 + yU_3, \\ u_y = V_1 + xV_2 + yV_3, \\ u_z = W_1 + xW_2 + yW_3, \end{cases} \tag{4}$$

where the unknown parameters on the right hand side (U_1, V_1, W_1, U_2, ..., W_3) represent the components of the generalized displacement vector. As a high-order

Table 1 MacLaurin's polynomials

N	n	ψ_i
0	1	$\psi_1=1$
1	3	$\psi_2=x$, $\psi_3=y$
2	6	$\psi_4=x^2$, $\psi_5=xy$, $\psi_6=y^2$
3	10	$\psi_7=x^3$, $\psi_8=x^2y$, $\psi_9=xy^2$, $\psi_{10}=y^3$
…	…	…
N	$(N+1)(N+2)/2$	$\psi_{(N^2+N+2)/2}=x^N$, $\psi_{(N^2+N+4)/2}=x^{N-1}y,\ldots,\psi_{N(N+3)/2}=xy^{N-1}$, $\psi_{(N+1)(N+2)/2}=y^N$

beam theory, high-order terms may be necessary as considered in Eq. (3). For instance, the three-order (N=3) kinematic field is expressed as follows:

$$\begin{aligned}
u_x &= U_1 + xU_2 + yU_3 + x^2U_4 + xyU_5 + y^2U_6 \\
&\quad x^3U_7 + x^2yU_8 + xy^2U_9 + y^3U_{10}, \\
u_y &= V_1 + xV_2 + yV_3 + x^2V_4 + xyV_5 + y^2V_6 \\
&\quad x^3V_7 + x^2yV_8 + xy^2V_9 + y^3V_{10}, \\
u_z &= W_1 + xW_2 + yW_3 + x^2W_4 + xyW_5 + y^2W_6 \\
&\quad x^3W_7 + x^2yW_8 + xy^2W_9 + y^3W_{10}.
\end{aligned} \tag{5}$$

In the cylindrical coordinate system, the position of an arbitrary point is easier to express and the following formulations are conveniently derived in modeling the stepped main shaft. Therefore, the main shaft model is established in the cylindrical coordinate system in this work. According to the establishing mode of the Cartesian coordinate system and the cylindrical coordinate system (Fig. 2), the displacement and coordinate relationship of the arbitrary point M between the two coordinate systems are expressed as

$$\begin{Bmatrix} u_x \\ u_y \\ u_z \end{Bmatrix} = \begin{bmatrix} \cos\varphi & -\sin\varphi & 0 \\ \sin\varphi & \cos\varphi & 0 \\ 0 & 0 & 1 \end{bmatrix} \begin{Bmatrix} u_\rho \\ u_\varphi \\ u_z \end{Bmatrix}, \tag{6}$$

$$\begin{cases} x = \rho\cos\varphi, \\ y = \rho\sin\varphi. \end{cases} \tag{7}$$

The displacement field of the model in the cylindrical coordinate system is transformed by substituting Eqs. (6) and (7) into Eq. (3):

$$\boldsymbol{u}(\rho,\varphi,z) = \boldsymbol{\psi}(\rho,\varphi)\boldsymbol{U}(z), \tag{8}$$

where $\boldsymbol{u}(\rho, \varphi, z)=[u_\rho(\rho, \varphi, z)\ u_\varphi(\rho, \varphi, z)\ u_z(\rho, \varphi, z)]^{\mathrm{T}}$ is the transposed displacement vector in the cylindrical coordinate system;

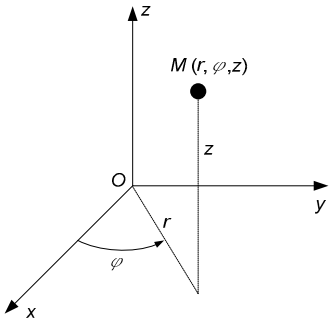

Fig. 2 Transformation of coordinates between the two coordinate systems

$$\boldsymbol{\psi} = \begin{bmatrix} \boldsymbol{\omega}_{11} & \boldsymbol{\omega}_{12} & \\ \boldsymbol{\omega}_{21} & \boldsymbol{\omega}_{22} & \\ & & \boldsymbol{\omega}_{33} \end{bmatrix}. \tag{9}$$

Note that $\boldsymbol{\omega}_{ij}$ is the row vector associated with section parameters ρ, φ only and the axial generalized displacements vector $\boldsymbol{U}$ is described by

$$\boldsymbol{U} = [U_1, U_2, \cdots, U_n,\ V_1, V_2, \cdots, V_n,\ W_1, W_2, \cdots, W_n]^{\mathrm{T}}, \tag{10}$$

where n=(N+1)(N+2)/2.

4 Finite element formulation

4.1 Preliminaries

Let us consider the cylindrical coordinate system shown in Fig. 2 for a circular shaft. The longitudinal axis of the circular shaft is the same as in the Cartesian coordinate system and the cross-section is defined by the radial coordinate ρ and the tangential coordinate φ. Referring to classical elasticity, the strain $\boldsymbol{\varepsilon}$ and the stress $\boldsymbol{\sigma}$ components in cylindrical coordinates are expressed as follows:

$$\begin{aligned}\boldsymbol{\varepsilon}&=[\varepsilon_\rho \quad \varepsilon_\varphi \quad \varepsilon_z \quad \gamma_{\rho\varphi} \quad \gamma_{\rho z} \quad \gamma_{\varphi z}]^{\mathrm{T}},\\ \boldsymbol{\sigma}&=[\sigma_\rho \quad \sigma_\varphi \quad \sigma_z \quad \tau_{\rho\varphi} \quad \tau_{\rho z} \quad \tau_{\varphi z}]^{\mathrm{T}}.\end{aligned} \tag{11}$$

A linear behavior can be assumed in case of small displacements, and then the strain-displacement relations are given by

$$\boldsymbol{\varepsilon}=\boldsymbol{B}\boldsymbol{u}, \tag{12}$$

where the linear differential operator $\boldsymbol{B}$ is defined as follows:

$$\begin{aligned}\boldsymbol{B}&=\begin{bmatrix}\boldsymbol{B}_1\\ \boldsymbol{B}_2\end{bmatrix},\\ \boldsymbol{B}_1&=\begin{bmatrix}\dfrac{\partial}{\partial\rho} & 0 & 0\\ \dfrac{1}{\rho} & \dfrac{1}{\rho}\dfrac{\partial}{\partial\varphi} & 0\\ 0 & 0 & \dfrac{\partial}{\partial z}\end{bmatrix},\\ \boldsymbol{B}_2&=\begin{bmatrix}\dfrac{1}{\rho}\dfrac{\partial}{\partial\varphi} & \dfrac{\partial}{\partial\rho}-\dfrac{1}{\rho} & 0\\ \dfrac{\partial}{\partial z} & 0 & \dfrac{\partial}{\partial\rho}\\ 0 & \dfrac{\partial}{\partial z} & \dfrac{1}{\rho}\dfrac{\partial}{\partial\varphi}\end{bmatrix}.\end{aligned} \tag{13}$$

The stress matrix can be obtained easily by the constitutive law:

$$\boldsymbol{\sigma}=\boldsymbol{D}\boldsymbol{\varepsilon}, \tag{14}$$

where the constitutive matrix $\boldsymbol{D}$ can be written as

$$\boldsymbol{D}=\begin{bmatrix}\lambda+2\mu & \lambda & \lambda & 0 & 0 & 0\\ \lambda & \lambda+2\mu & \lambda & 0 & 0 & 0\\ \lambda & \lambda & \lambda+2\mu & 0 & 0 & 0\\ 0 & 0 & 0 & \mu & 0 & 0\\ 0 & 0 & 0 & 0 & \mu & 0\\ 0 & 0 & 0 & 0 & 0 & \mu\end{bmatrix}, \tag{15}$$

where λ and μ are Lame's parameters denoted by the elastic modulus E and Poisson's ratio v.

$$\begin{aligned}\lambda&=\frac{Ev}{(1+v)(1-2v)},\\ \mu&=\frac{E}{2(1+v)}.\end{aligned} \tag{16}$$

4.2 Fundamental nuclei

The finite element method is used to discretize the shaft along its axis. The generalized displacement is interpolated by employing the shape functions $N_\tau(z)$:

$$\boldsymbol{u}(\rho,\varphi,z)=\psi_i(\rho,\varphi)N_\tau(z)\boldsymbol{d}_{i\tau}, \tag{17}$$

where $\boldsymbol{d}_{i\tau}$ is the nodal unknown vector. The expression and properties of the shape function are not specified in this study, but more detailed explanation can be found in (Bathe, 1996). One-dimensional beam elements with two nodes have been used in this work. This means that a linear approximation was assumed along the z axis. The governing differential equations and the associated natural boundary conditions were obtained via the principle of minimum potential energy:

$$\delta\Pi=\delta U+\delta U_{\mathrm{P}}=0, \tag{18}$$

where Π is the total potential energy of elements and δ is the virtual variation. U and U_{P} are the strain energy and the potential energy of elements, respectively. Their expressions are given as follows:

$$\delta U=\frac{1}{2}\delta\int_l\int_A\boldsymbol{\varepsilon}^{\mathrm{T}}\boldsymbol{\sigma}\mathrm{d}A\mathrm{d}z, \tag{19}$$

$$\delta U_{\mathrm{P}}=-\int_l\int_A\delta\boldsymbol{u}^{\mathrm{T}}\boldsymbol{p}\mathrm{d}A\mathrm{d}z-\int_A\delta\boldsymbol{u}^{\mathrm{T}}\boldsymbol{q}\mathrm{d}A, \tag{20}$$

where the integral interval l is the length of a discrete element and A is the area of the cross-section. It should be noted that $\boldsymbol{p}$ stands for volume force and $\boldsymbol{q}$ stands for surface force, both components being defined on the basis of an element.

$$\begin{aligned}\boldsymbol{p}&=[p_\rho \quad p_\varphi \quad p_z]^{\mathrm{T}},\\ \boldsymbol{q}&=[q_\rho \quad q_\varphi \quad q_{\rho\varphi}]^{\mathrm{T}}.\end{aligned} \tag{21}$$

The governing differential equations are obtained by substituting Eqs. (12), (14), and (17) into Eqs. (19) and (20):

$$\int_l\int_A N_\tau\psi_i \boldsymbol{B}^{\mathrm{T}}\boldsymbol{D}\boldsymbol{B}\psi_j N_s \mathrm{d}A\mathrm{d}z\boldsymbol{d}_{js} = \int_l\int_A N_\tau\psi_i \boldsymbol{p}\mathrm{d}A\mathrm{d}z + \int_A N_\tau\psi_i \boldsymbol{q}\mathrm{d}A, \tag{22}$$

where the shape function N_s and the expansion function ψ_j are related to the nodal unknown vector $\boldsymbol{d}_{js}$; the four subscripts i, j, τ, and s are the indexes to expand the elemental matrix.

According to Eq. (22), the elemental stiffness matrix and the loading vector are written as

$$\boldsymbol{k}^{ij\tau s} = \int_l\int_A N_\tau\psi_i \boldsymbol{B}^{\mathrm{T}}\boldsymbol{D}\boldsymbol{B}\psi_j N_s \mathrm{d}A\mathrm{d}z, \tag{23}$$

$$\boldsymbol{f}^{\tau i} = \int_l\int_A N_\tau\psi_i \boldsymbol{p}\mathrm{d}A\mathrm{d}z + \int_A N_\tau\psi_i \boldsymbol{q}\mathrm{d}A, \tag{24}$$

where $\boldsymbol{k}^{ij\tau s}$ is the stiffness matrix, which is described in the form of the fundamental nuclei and does not depend on the expansion order. The stiffness matrix is a 3×3 matrix and contains nine differential operators:

$$\boldsymbol{k}^{ij\tau s} = \begin{bmatrix} k_{\rho\rho}^{ij\tau s} & k_{\rho\varphi}^{ij\tau s} & k_{\rho z}^{ij\tau s} \\ k_{\varphi\rho}^{ij\tau s} & k_{\varphi\varphi}^{ij\tau s} & k_{\varphi z}^{ij\tau s} \\ k_{z\rho}^{ij\tau s} & k_{z\varphi}^{ij\tau s} & k_{zz}^{ij\tau s} \end{bmatrix}. \tag{25}$$

The nine components are listed as follows:

$$k_{\rho\rho}^{ij\tau s} = (\lambda+2\mu)\left\{\int_l N_\tau N_s\mathrm{d}z\int_A \psi_{i,\rho}\psi_{j,\rho}\mathrm{d}A + \int_V \frac{1}{\rho^2}\mathrm{d}V\right\} + \lambda\int_l N_\tau N_s\mathrm{d}z\int_A \frac{1}{\rho}\left(\psi_{i,\rho}\psi_j + \psi_i\psi_{j,\rho}\right)\mathrm{d}A + \mu\left\{\int_l N_\tau N_s\mathrm{d}z\int_A \frac{1}{\rho^2}\psi_{i,\varphi}\psi_{j,\varphi}\mathrm{d}A + \int_l N_{\tau,z}N_{s,z}\mathrm{d}z\int_A \psi_i\psi_j\mathrm{d}A\right\},$$

$$k_{\rho\varphi}^{ij\tau s} = (\lambda+2\mu)\int_l N_\tau N_s\mathrm{d}z\int_A \frac{1}{\rho^2}\psi_i\psi_{j,\varphi}\mathrm{d}A + \lambda\int_l N_\tau N_s\mathrm{d}z\int_A \frac{1}{\rho}\left(\psi_{i,\varphi}\psi_{j,\rho}\right)\mathrm{d}A + \mu\left\{\int_l N_\tau N_s\mathrm{d}z\int_A \frac{1}{\rho}\psi_{i,\varphi}\psi_{j,\rho}\mathrm{d}A - \int_l N_\tau N_s\mathrm{d}z\int_A \frac{1}{\rho^2}\psi_{i,\varphi}\psi_j\mathrm{d}A\right\},$$

$$k_{\rho z}^{ij\tau s} = \lambda\left\{\int_l N_\tau N_{s,z}\mathrm{d}z\int_A \psi_{i,\rho}\psi_j\mathrm{d}A + \int_l N_\tau N_{s,z}\mathrm{d}z\int_A \frac{1}{\rho}\psi_i\psi_j\mathrm{d}A\right\} + \mu\int_l N_{\tau,z}N_s\mathrm{d}z\int_A \frac{1}{\rho^2}\psi_i\psi_{j,\rho}\mathrm{d}A,$$

$$k_{\varphi\rho}^{ij\tau s} = (\lambda+2\mu)\int_l N_\tau N_s\mathrm{d}z\int_A \frac{1}{\rho^2}\psi_i\psi_{j,\varphi}\mathrm{d}A + \lambda\int_l N_\tau N_s\mathrm{d}z\int_A \frac{1}{\rho}\left(\psi_{i,\rho}\psi_{j,\varphi}\right)\mathrm{d}A + \mu\left\{\int_l N_\tau N_s\mathrm{d}z\int_A \frac{1}{\rho}\psi_{i,\rho}\psi_{j,\varphi}\mathrm{d}A - \int_l N_\tau N_s\mathrm{d}z\int_A \frac{1}{\rho^2}\psi_{i,\varphi}\psi_j\mathrm{d}A\right\},$$

$$k_{\varphi\varphi}^{ij\tau s} = (\lambda+2\mu)\int_l N_\tau N_s\mathrm{d}z\int_A \frac{1}{\rho^2}\psi_{i,\varphi}\psi_{j,\varphi}\mathrm{d}A + \mu\left\{\int_l N_\tau N_s\mathrm{d}z\int_A \frac{1}{\rho^2}\psi_i\psi_j\mathrm{d}A + \int_l N_\tau N_s\mathrm{d}z\int_A \psi_{i,\rho}\psi_{j,\rho}\mathrm{d}A - \int_l N_\tau N_s\mathrm{d}z\int_A \frac{1}{\rho}\left(\psi_{i,\rho}\psi_j + \psi_i\psi_{j,\rho}\right)\mathrm{d}A + \int_l N_{\tau,z}N_{s,z}\mathrm{d}z\int_A \psi_i\psi_j\mathrm{d}A\right\},$$

$$k_{\varphi z}^{ij\tau s} = \lambda\int_l N_\tau N_{s,z}\mathrm{d}z\int_A \frac{1}{\rho}\psi_{i,\varphi}\psi_j\mathrm{d}A + \mu\int_l N_{\tau,z}N_s\mathrm{d}z\int_A \frac{1}{\rho}\psi_i\psi_{j,\varphi}\mathrm{d}A,$$

$$k_{z\rho}^{ij\tau s} = \lambda\left\{\int_l N_\tau N_{s,z}\mathrm{d}z\int_A \psi_{i,\rho}\psi_j\mathrm{d}A + \int_l N_\tau N_{s,z}\mathrm{d}z\int_A \frac{1}{\rho}\psi_i\psi_j\mathrm{d}A\right\} + \mu\int_l N_{\tau,z}N_s\mathrm{d}z\int_A \frac{1}{\rho^2}\psi_i\psi_{j,\rho}\mathrm{d}A,$$

$$k_{z\varphi}^{ij\tau s} = \lambda\int_l N_\tau N_{s,z}\mathrm{d}z\int_A \frac{1}{\rho}\psi_{i,\varphi}\psi_j\mathrm{d}A + \mu\int_l N_{\tau,z}N_s\mathrm{d}z\int_A \frac{1}{\rho}\psi_i\psi_{j,\varphi}\mathrm{d}A,$$

$$k_{zz}^{ij\tau s} = (\lambda+2\mu)\int_l N_{\tau,z}N_{s,z}\mathrm{d}z\int_A \psi_i\psi_j\mathrm{d}A + \mu\left\{\int_l N_\tau N_s\mathrm{d}z\int_A \frac{1}{\rho^2}\psi_{i,\varphi}\psi_{j,\varphi}\mathrm{d}A + \int_l N_\tau N_s\mathrm{d}z\int_A \psi_{i,\rho}\psi_{j,\rho}\mathrm{d}A\right\}.$$

Global integration of the stiffness matrices of the main shaft model is based on the four indices i, j, τ, and s which are associated with the expansion functions and the shape functions. For more detail on the expansion of nuclei and assembly procedures in FEM framework, please refer to (Carrera et al., 2014).

The governing differential equations are achieved for static analysis by expanding $\boldsymbol{k}^{ij\tau s}$:

$$\boldsymbol{KD} = \boldsymbol{F}, \tag{26}$$

where $\boldsymbol{K}$ stands for the assembled stiffness matrix and $\boldsymbol{F}$ stands for the nodal loading vector.

5 Numerical results and experimental tests

The accuracy and availability of the present beam theory are demonstrated by implementing the static analysis of the stepped main shaft model and the field experiment of the main shaft in Zhaojiazhai Coal Mine, China and the results are presented in this section. First, static analysis of a single shaft part is addressed in order to show the convergence rate and the accuracy of the refined beam theory. Research on the relation between displacements and slender ratio S of shaft parts is also conducted using numerical simulation. Next, the main shaft model is analyzed to make a comparison between the present beam model and the ANSYS solid model. Finally, the static analysis of the main shaft model is compared with the results of the field experiment so as to validate the availability of the present beam theory.

5.1 Static analysis of the single shaft part

A solid circular cross-section beam with a fixed-free condition was applied to study the convergence of the refined beam theory under the two different loading cases (Fig. 3). A single force F_y (F_y=−1000 N) and a torque T (T=100 N·m) are applied at the end of the beam. The circular cross-section and the load are shown in Fig. 4, and the point of force application is at (0, 0, L). The length and radius are denoted by L (L=1 m) and r, respectively. Note that the slender ratio mentioned below is maintaining the same length. The main shaft is made of a steel alloy whose material parameters are: Young's modulus E=200 GPa and Poisson's ratio ν=0.3.

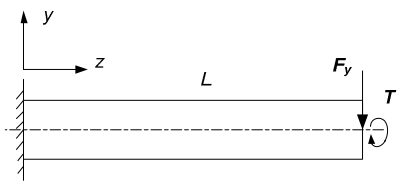

Fig. 3 Simply supported beam undergoing two different load at the free end

Table 2 shows the convergence analysis for the circular cross-section beam undergoing a single force F_y by considering both the slender ratio and the order of the TE model. The convergence of different order models for different slender ratio is found in this table, which results from the same length of beam model. The stable displacement value can be obtained by employing 40 finite elements as shown in Table 2. In the course of modeling the structure shown in

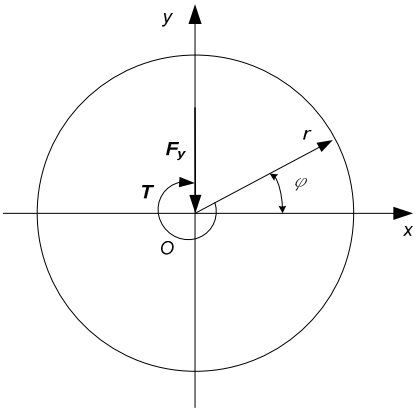

Fig. 4 Circular cross-section geometry, load, and verification points

Table 2 Radial displacement at (0, 0, L) for the fixed-free circular cross-section beam with different slender ratios

Numbers of elements	u_ρ (×10^{-6} m)			
	N=1	N=2	N=3	N=4
S=2				
1	0.0303	0.0338	0.0350	0.0368
3	0.0401	0.0483	0.0501	0.0541
5	0.0411	0.0510	0.0528	0.0577
10	0.0416	0.0526	0.0543	0.0601
40	0.0418	0.0532	0.0549	0.0613
80	0.0418	0.0532	0.0549	0.0614
S=5				
1	0.322	0.337	0.338	0.340
3	0.861	0.999	1.008	1.014
5	0.994	1.216	1.227	1.236
10	1.063	1.348	1.361	1.373
40	1.087	1.401	1.414	1.432
80	1.088	1.404	1.417	1.436
S=10				
1	1.54	1.56	1.56	1.56
3	7.86	8.63	8.64	8.65
5	11.72	13.82	13.85	13.86
10	14.77	18.67	18.75	18.77
40	16.08	21.15	21.22	21.26
80	16.15	21.30	21.37	21.42

Fig. 3, 40 equal elements are used in the TE models, while the SOLID 186 20-node element is used in the ANSYS simulation in the following static analysis.

Table 3 shows displacement components at the verification points for different slender ratio beams under a single force F_y. Classical and second-order TE models as well as ANSYS solid models are given in Table 3. Considering the influence of Poisson locking and the lower computational effort, the second-order TE model is chosen here for comparison purposes. The displacement values of the second-order TE model are closer to ANSYS Solid theory than classical beam theories for different slender ratio. It is interesting that the demarcation value of slender ratio is 4. That is to say, the classical beam theories cannot achieve reasonable results compared to the ANSYS solid model and the TE model is suitable when the slender ratio is less than 4.

Radial and axial displacements at (0, 0, L) for a circular cross-section beam are provided in Table 4, together with the number of degrees of freedom (DOFs) for each model employed. Classical and four TE models as well as the ANSYS solid model are presented in the table. The ANSYS solid model is used as comparative values in this study.

Table 5 shows radial displacement and axial stress at (r/2, 0, L/2) for a circular cross-section beam with different slender ratios. Table 6 shows tangential

Table 3 Displacement components at the verification points for different slender ratio beams

Model		u_φ ($\times10^{-6}$ m)										
		S=1	S=2	S=3	S=4	S=5	S=7	S=10	S=15	S=20	S=30	S=40
EBBM		0.0106	0.0849	0.286	0.679	1.33	3.64	10.6	35.8	84.9	286	679
TBM		0.0340	0.132	0.357	0.772	1.44	3.80	10.8	36.2	85.3	287	680
(0, 0, L)	ANSYS	0.252	0.347	0.566	0.973	1.63	3.96	10.9	36.1	85.0	286	678
	TE, N=2	0.0419	0.133	0.348	0.749	1.40	3.72	10.7	35.6	84.0	280	656
(r, π, L)	ANSYS	0.0188	0.112	0.331	0.738	1.40	3.72	10.7	35.8	84.8	286	678
	TE, N=2	0.0123	0.103	0.317	0.720	1.37	3.69	10.6	35.6	83.9	280	656
(r, π/2, L)	ANSYS	0.0291	0.124	0.343	0.749	1.41	3.74	10.7	35.9	84.8	286	678
	TE, N=2	0.0253	0.116	0.331	0.734	1.39	3.70	10.6	35.6	83.9	280	656

Table 4 Radial and axial displacements at (0, 0, L) for a circular cross-section beam, S=1, 2, 4

Model	S=1		S=2		S=4		DOFs
	$-u_\rho$ ($\times10^{-9}$ m)	u_z ($\times10^{-9}$ m)	$-u_\rho$ ($\times10^{-9}$ m)	u_z ($\times10^{-9}$ m)	$-u_\rho$ ($\times10^{-9}$ m)	u_z ($\times10^{-9}$ m)	
EBBM	2.12	–	33.95	–	543.25	–	123
TBM	6.79	–	52.63	–	617.95	–	205
TE, N=1	5.71	2.36	41.76	18.91	469.32	151.19	369
TE, N=2	5.07	2.90	46.56	24.35	586.38	198.70	738
TE, N=3	5.49	2.99	48.55	24.57	595.23	199.38	1230
TE, N=4	6.07	3.00	49.80	24.62	598.38	199.57	1845
ANSYS	5.97	3.05	49.78	24.78	599.87	200.12	99720 (min.)

Table 5 Radial displacement and axial stress at (r/2, 0, L/2) for a circular cross-section beam, S=1, 2, 4

Model	S=1		S=2		S=4	
	u_ρ ($\times10^{-9}$ m)	$-\sigma_z$ (Pa)	u_ρ ($\times10^{-9}$ m)	$-\sigma_z$ (Pa)	u_ρ ($\times10^{-9}$ m)	$-\sigma_z$ (Pa)
TE, N=1	2.562	326.25	16.154	2609.52	159.064	20861.26
TE, N=2	2.926	327.25	18.439	2626.55	195.597	21027.69
TE, N=3	3.105	375.27	19.410	2672.35	200.092	21041.18
TE, N=4	3.284	481.92	19.712	2702.73	201.077	21020.65
ANSYS	3.434	535.91	19.879	2782.86	201.943	20414.29

displacement and shearing stress at (r, 0, L/2) for the circular cross-section beam under pure torque-loading. Both tables provide four TE models and the ANSYS solid model for comparison.

Fig. 5 shows the distribution of the shearing stress field on the cross-section of z=L/2 for different

Table 6 Tangential displacement and shearing stress at (r, 0, L/2) for a circular cross-section beam under pure torque-loading

Model	S=1		S=2		S=4	
	u_φ ($\times10^{-9}$ m)	$\sigma_{\varphi z}$ (Pa)	u_φ ($\times10^{-9}$ m)	$\sigma_{\varphi z}$ (Pa)	u_φ ($\times10^{-9}$ m)	$\sigma_{\varphi z}$ (Pa)
TE, N=1	0.414	63.66	3.310	509.30	26.483	4074.37
TE, N=2	0.414	63.66	3.310	509.30	26.483	4074.37
TE, N=3	0.414	63.66	3.310	509.30	26.483	4074.37
TE, N=4	0.414	63.66	3.310	509.30	26.483	4074.37
ANSYS	0.414	63.79	3.310	510.34	26.483	4082.73

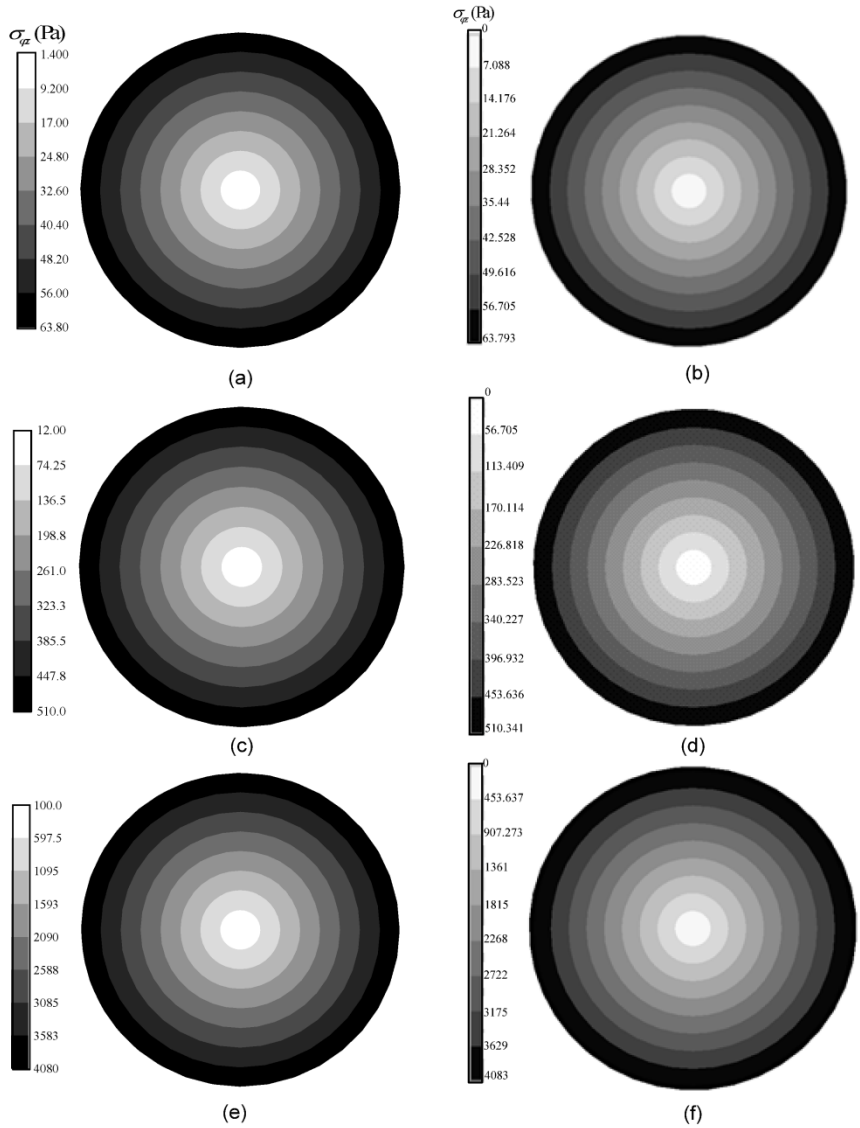

Fig. 5 Comparison of shearing stress field (Pa) at z=L/2 for different slender ratios between TE models and ANSYS solid model: (a) S=1, TE (N=1, 2, 3, 4) model; (b) S=1, ANSYS solid model; (c) S=2, TE (N=1, 2, 3, 4) model; (d) S=2, ANSYS solid model; (e) S=4, TE (N=1, 2, 3, 4) model; (f) S=4, ANSYS solid model

slender ratios with pure torque-loading. TE models are compared with the 3D solution from ANSYS. Figs. 6–8 show the distribution of axial stress field on the cross-section of $z=L/2$ for different slender ratios

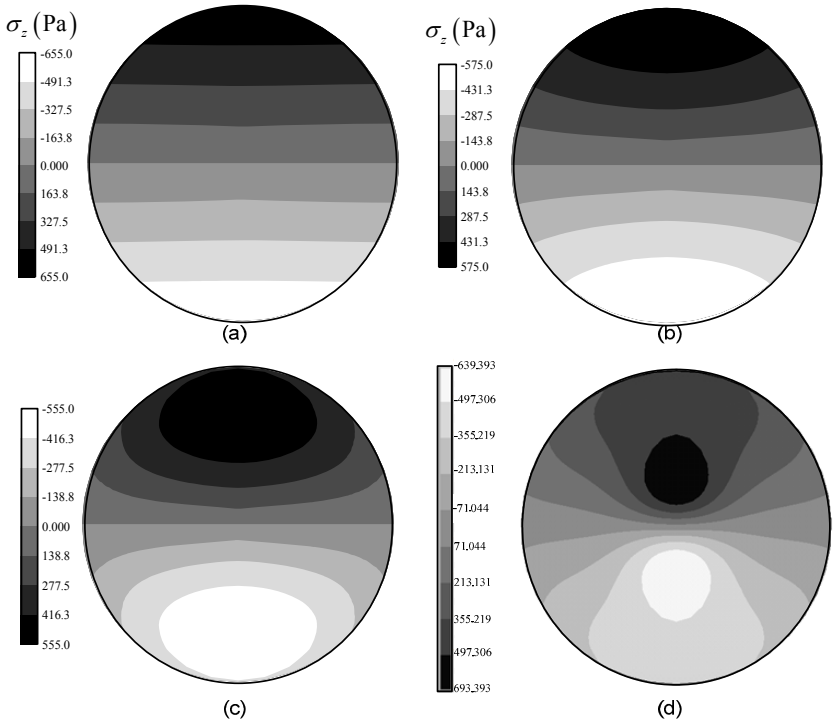

Fig. 6 Comparison of axial stress field (Pa) at $z=L/2$ for $S=1$ beam between TE models and ANSYS solid model
(a) TE (N=1) model; (b) TE (N=3) model; (c) TE (N=4) model; (d) ANSYS solid model

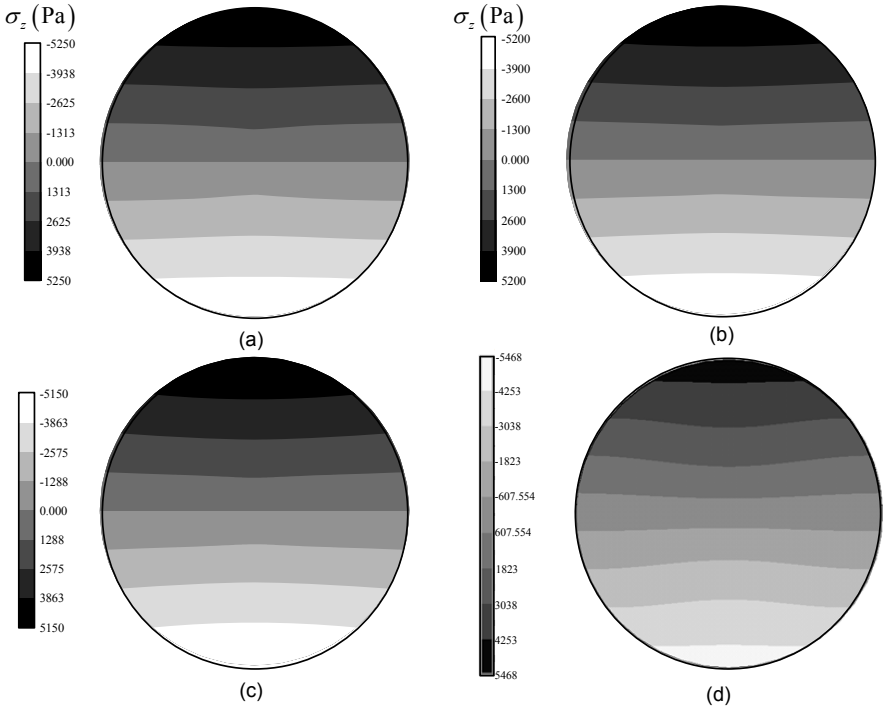

Fig. 7 Comparison of axial stress field (Pa) at $z=L/2$ for $S=2$ beam between TE models and ANSYS solid model
(a) TE (N=1) model; (b) TE (N=3) model; (c) TE (N=4) model; (d) ANSYS solid model

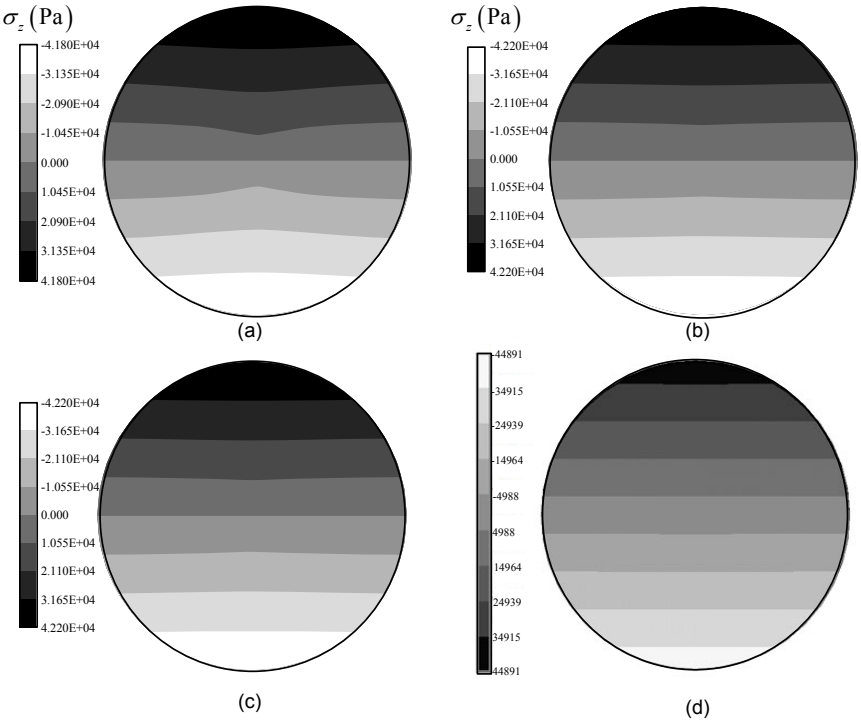

Fig. 8 Comparison of axial stress field (Pa) at $z=L/2$ for $S=4$ beam between TE models and ANSYS solid model
(a) TE (N=1) model; (b) TE (N=3) model; (c) TE (N=4) model; (d) ANSYS solid model

with a single force. TE (N=1, 3, 4) models are compared with ANSYS solid models in each figure.

The main conclusions from the analysis are:

1. Classical (EBBM, TBM) and lower-order TE models cannot detect localized displacement values and stress values accurately, particularly when the slender ratio is less than 4.

2. High-order TE models can provide results closer to the ANSYS solid model with very low computational effort.

3. For the pure torque-loading, TE models can obtain results exactly independent of the order of model.

5.2 Analysis of the modified main shaft model and experiment

The real structure of the multiple-rope friction mining hoist is shown in Fig. 9, together with the diagram of the inner structure. As shown in Fig. 9b, the multiple-rope friction mining hoist includes a friction wheel, main shaft, and two main bearings. Just as its name implies, there are four wire ropes hanging on the friction wheel equally spaced in the axial direction. The four wire ropes are attached to hoisting containers used to transport the workers, related equipment, and tools. When the multiple-rope friction mining hoist operates the main shaft is subjected to transverse force and torque. In the Zhaojiazhai Coal Mine, the main parameters of the hoist system are shown in Table 7.

The main shaft plays a vital role in undergoing load and transmission in the mine hoist. The mechanical structure of the main shaft is shown in Fig. 10. The shaft has 11 shaft-segments of different lengths and radii. It is noted that segments 4 and 6 are flanged and connect with the friction wheel using high-strength bolts. Two main bearings are installed on segments 1 and 8 of the main shaft and the motor rotor is fixed on segments 10 and 11 with mechanical position limitation. The geometric parameters of each segment of the main shaft are given in Table 8. The present theory is suitable for modeling the main shaft because every shaft-segment's slender ratio is no more than 4.

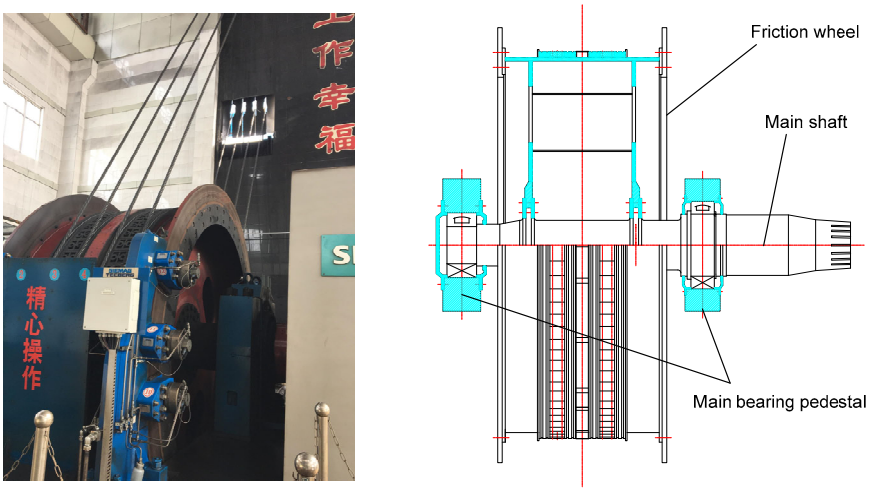

Fig. 9 Multiple-rope friction mining hoist
(a) Real structure; (b) Diagram of inner structure

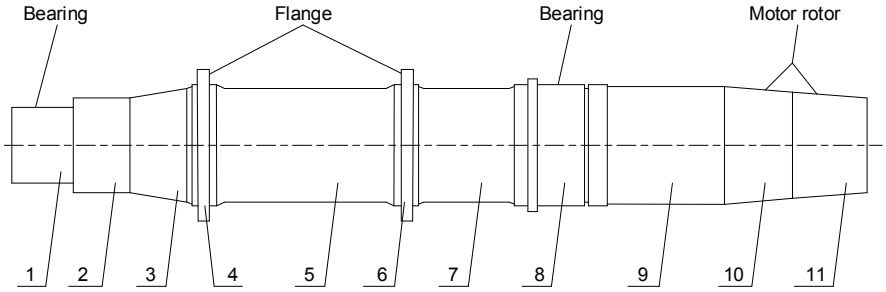

Fig. 10 Mechanical structure of the main shaft of the friction mining hoist used in the Zhaojiazhai Coal Mine, China

Table 7 Main parameters of the hoist system in the Zhaojiazhai Coal Mine, China

Property	Value
Weight of the skip, m_s (kg)	33 500
Rated payload, m_p (kg)	22 000
Equivalent mass of the friction wheel, m_{ef} (t)	22.1
Rotational inertia of the hoister, J_h (t·m^2)	88.4
Rated acceleration and deceleration, a (m/s^2)	0.7
Rotational inertia of motor, J_m (t·m^2)	20

The transverse forces F_e and torque T_e are calculated by

$$F_e = m_p g + 2m_s g + m_p a + m_{ef} g, \tag{27}$$

$$T_e = m_p gR + 2m_s a + J_h \frac{a}{R} + J_m \frac{a}{R}. \tag{28}$$

Then the surface forces $\boldsymbol{q}_f$ and $\boldsymbol{q}_m$ can be expressed as

Table 8 Geometric parameters of each segment of the main shaft

n	r (mm)	L (mm)	S
1	240.0	330	1.375
2	300.0	300	1.000
3	307.5	280	0.910
4	482.5	65	0.135
5	322.5	1310	4.000
6	485.0	65	0.134
7	322.5	470	1.460
8	400.0	258	0.645
9	390.0	660	1.540
10	382.5	180	0.470

$$F_e = \int_{A_l} N_\tau \psi_i \boldsymbol{q}_f \mathrm{d}A_l, \tag{29}$$

$$T_{\mathrm{e}}=\int_{A_2} N_\tau \psi_i \boldsymbol{q}_{\mathrm{m}} \mathrm{d}A_2, \tag{30}$$

where A_1 and A_2 are force bearing area and the area of friction surface, respectively.

To simplify the model of the main shaft shown in Fig. 10 and reduce computational cost, we studied the influence of generalized coordinates exerted on the strain field. The nodal generalized displacements are numbered 1 to 18 for brevity. The influence coefficient is given by

$$S_i=\frac{\Delta\varepsilon}{\Delta d_i}, \tag{31}$$

where $\Delta\varepsilon$ stands for strain variation and Δd_i for the ith nodal generalized displacement variation.

Fig. 11 shows the influence coefficient S_i of the ith generalized coordinate exerted on the strain field undergoing a different load. The bar filling with cross-hatching represents the influence coefficient of the nodal generalized displacements on the value of strain under torque and transverse loading conditions. From Fig. 11, the generalized displacements numbered 1, 2, 4, 6, 9, and 11 make much more contribution under transverse load condition and 3 and 8 have much more effect under the torque condition. It is clear that the generalized displacements 12 to 18 have no impact on the strain field and 1 to 12 need to be considered. That is to say the radial displacement variation and the tangential displacement variation play a role in the influence of the strain.

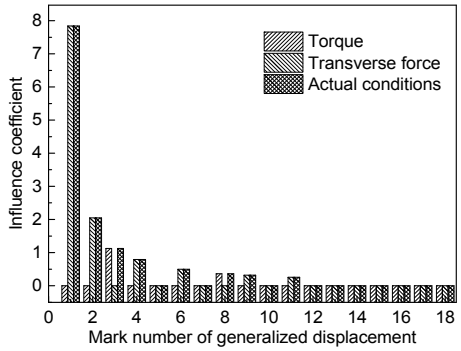

Fig. 11 Influence coefficient of generalized coordinates exerted on the strain field

Accordingly, the element generalized displacements can be written as

$$U_5=V_1=V_4=V_6=0,\ W_j=0,\ j=1,2,3,4,5,6. \tag{32}$$

Then the nodal displacement vector is modified as

$$\boldsymbol{d}=\boldsymbol{R}\bar{\boldsymbol{d}}, \tag{33}$$

where the modified matrix is constructed as

$$\boldsymbol{R}=\begin{bmatrix}\boldsymbol{R}_0 & \boldsymbol{0}\\ \boldsymbol{0} & \boldsymbol{R}_0\end{bmatrix},\ \boldsymbol{R}_0=\begin{bmatrix}\boldsymbol{R}_1 & \boldsymbol{0}\end{bmatrix},$$

$$\boldsymbol{R}_1=\begin{bmatrix}1&0&0&0&0&0&0&0&0&0&0\\0&1&0&0&0&0&0&0&0&0&0\\0&0&1&0&0&0&0&0&0&0&0\\0&0&0&1&0&0&0&0&0&0&0\\0&0&0&0&0&1&0&0&0&0&0\\0&0&0&0&0&0&0&1&0&0&0\\0&0&0&0&0&0&0&0&1&0&0\\0&0&0&0&0&0&0&0&0&0&1\end{bmatrix}.$$

Substituting Eq. (33) into Eq. (17), the element stiffness matrix and the loading vector become

$$\begin{aligned}\boldsymbol{k}&=\boldsymbol{R}^{\mathrm{T}}\bar{\boldsymbol{k}}\boldsymbol{R},\\ \boldsymbol{f}&=\bar{\boldsymbol{f}}\boldsymbol{R}.\end{aligned} \tag{34}$$

To verify the accuracy of the 1D higher-order model, a comparison is made between the fourth-order TE model and ANSYS solid model. The equivalent strain ε_{e} is defined as

$$\varepsilon_{\mathrm{e}}=\sqrt{\frac{2}{9}\left(\varepsilon_\rho^2+\varepsilon_\varphi^2+\varepsilon_z^2+\gamma_{\rho\varphi}^2+\gamma_{\rho z}^2+\gamma_{\varphi z}^2\right)}. \tag{35}$$

Figs. 12 and 13 show the equivalent strain ε_{e} contours on the surface of segment 7 of the main shaft for the two different loading cases: the constant speed status and the acceleration status. Comparison results show that the fourth-order TE model successfully detect complex stress/strain field in accordance with the 3D elasticity equations.

Owing to the limits of the maintenance and the regulations of coal mine production, we can only conduct the experiment in a light condition (m_{p}=0). As shown in Fig. 14, the experimental system employs a wireless transmitting and receiving module in

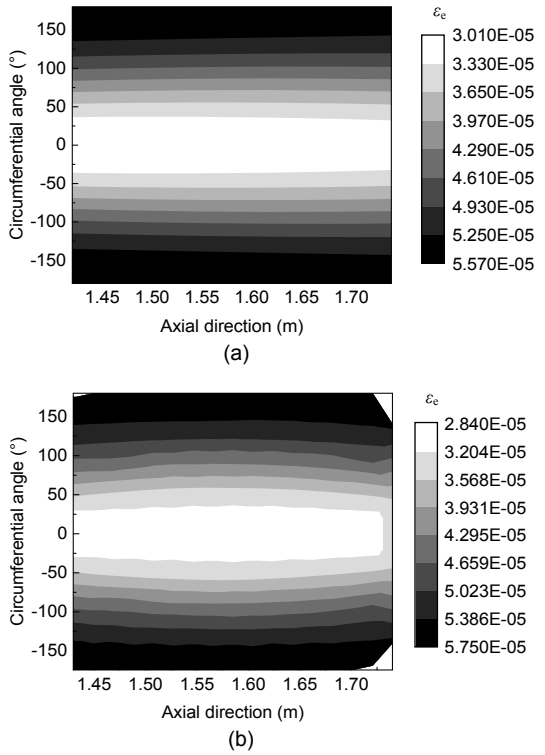

Fig. 12 Comparison of strain contours on the surface of segment 7 of the main shaft based on different models in constant speed status: (a) TE (N=4) model; (b) ANSYS solid model

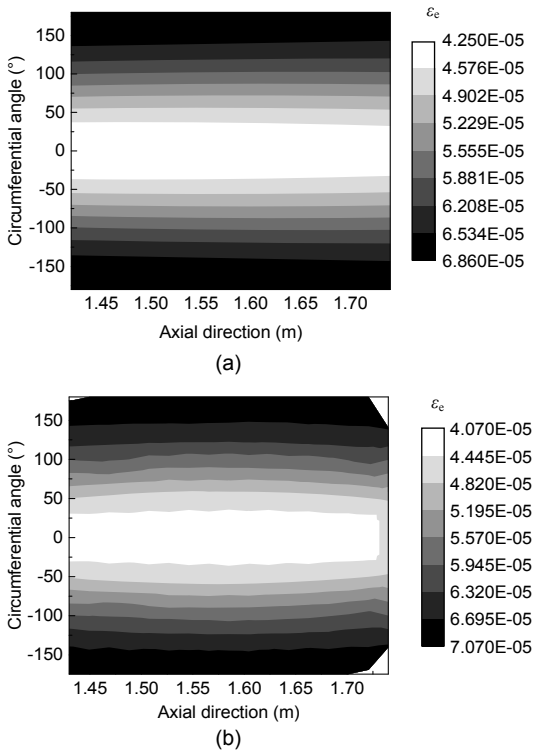

Fig. 13 Comparison of strain contours on the surface of segment 7 of the main shaft based on different models in acceleration status: (a) TE (N=4) model; (b) ANSYS solid model

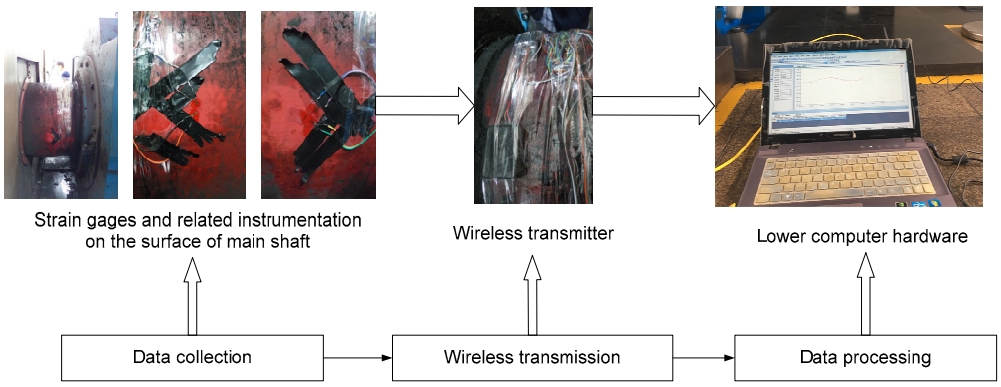

Fig. 14 Test system of dynamic behaviors of the main shaft

measuring strains on the surface of segment 9 of the main shaft. This includes measuring equipment and data-processing instrument.

In different working conditions, the load applied on the surface of the main shaft is constant. Therefore, the simulation results can be based on the static force analysis of the main shaft model. The curves of strains versus running time on the surface of segment 9 of the main shaft are depicted in Fig. 15, from which we can see that the results provided by the fourth-order TE model are consistent with the experimental results in the four different working conditions. The present theory is able to predict the strain field on the surface of the main shaft of the mining hoist satisfactorily.

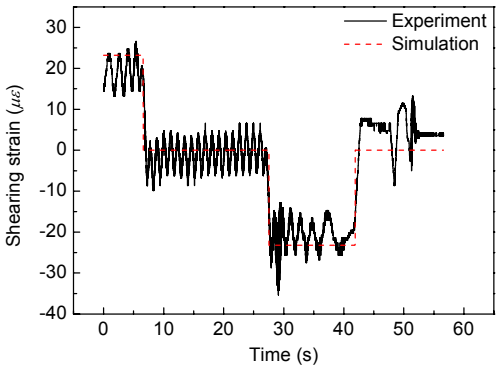

Fig. 15 Curves of shearing strain versus running time on the surface of segment 9 of the main shaft

6 Conclusions

The governing differential equations for the stepped main shaft have been deduced in the cylindrical coordinate system using the CUF, which are mainly used for the static analysis. The finite formulation of the governing differential equations has been implemented with the linear interpolation based on Taylor series. Finally, the 1D higher-order model was obtained by employing the principle of minimum potential energy and modified by studying the influence of generalized coordinates. Numerical results of the modified 1D higher-order model were obtained and compared with classical beam models, the ANSYS solid model, and experimental results. In the case of static analysis, the modified 1D higher-order model is in good agreement with the ANSYS solid model with much less computational effort and complexity. Finally, the practicability of the present model in predicting the strain field on the surface of the main shaft of the mine hoist has been validated by comparison with experimental results.

References

Bathe KJ, 1996. Finite Element Procedure. Prentice Hall, New Jersey, USA.

Carrera E, Giunta G, 2010. Refined beam theories based on a unified formulation. *International Journal of Applied Mechanics*, 2(1):117-143. https://doi.org/10.1142/S1758825110000500

Carrera E, Petrolo M, 2011. On the effectiveness of higher-order terms in refined beam theories. *Journal of Applied Mechanics*, 78(2):021013. https://doi.org/10.1115/1.4002207

Carrera E, Petrolo M, 2012. Refined beam elements with only displacement variables and plate/shell capabilities. *Meccanica*, 47(3):537-556. https://doi.org/10.1007/s11012-011-9466-5

Carrera E, Giunta G, Petrolo M, 2011. Beam Structures: Classical and Advanced Theories. John Wiley & Sons, Chichester, West Sussex, UK, p.188.

Carrera E, Cinefra M, Petrolo M, et al., 2014. Finite Element Analysis of Structures through Unified Formulation. John Wiley & Sons, Chichester, West Sussex, UK, p.385.

Carrera E, Pagani A, Petrolo M, et al., 2015a. Recent developments on refined theories for beams with applications. *Mechanical Engineering Reviews*, 2(2):1400298. https://doi.org/10.1299/mer.14-00298

Carrera E, Pagani A, Petrolo M, 2015b. Refined 1D finite elements for the analysis of secondary, primary, and complete civil engineering structures. *Journal of Structural Engineering*, 141(4):04014123. https://doi.org/10.1061/(ASCE)ST.1943-541X.0001076

Chan KT, Lai KF, Stephen NG, et al., 2011. A new method to determine the shear coefficient of Timoshenko beam theory. *Journal of Sound and Vibration*, 330(14):3488-3497. https://doi.org/10.1016/j.jsv.2011.02.012

Cowper GR, 1966. The shear coefficient in Timoshenko's beam theory. *Journal of Applied Mechanics*, 33(2):335-340. https://doi.org/10.1115/1.3625046

Dhillon BS, 2010. Mine Safety: a Modern Approach. Springer-Verlag London Limited, London, UK, p.192.

Euler L, 1744. De Curvis Elasticis. Bousquet, Geneva, Switzerland.

Filippi M, Pagani A, Petrolo M, et al., 2015. Static and free vibration analysis of laminated beams by refined theory based on Chebyshev polynomials. *Composite Structures*, 132:1248-1259. https://doi.org/10.1016/j.compstruct.2015.07.014

Friedman Z, Kosmatka JB, 1993. An improved two-node Timoshenko beam finite element. *Computers & Structures*, 47(3):473-481. https://doi.org/10.1016/0045-7949(93)90243-7

Gao XL, 2015. A new Timoshenko beam model incorporating microstructure and surface energy effects. *Acta Mechanica*, 226(2):457-474. https://doi.org/10.1007/s00707-014-1189-y

Gruttmann F, Wagner W, 2001. Shear correction factors in Timoshenko's beam theory for arbitrary shaped cross-sections. *Computational Mechanics*, 27(3):199-207. https://doi.org/10.1007/s004660100239

Hutchinson JR, 2001. Shear coefficients for Timoshenko beam theory. *Journal of Applied Mechanics*, 68(1):87-92. https://doi.org/10.1115/1.1349417

Jensen JJ, 1983. On the shear coefficient in Timoshenko's beam theory. *Journal of Sound and Vibration*, 87(4):621-635. https://doi.org/10.1016/0022-460X(83)90511-4

Pagani A, Boscolo M, Banerjee JR, et al., 2013. Exact dynamic

stiffness elements based on one-dimensional higher-order theories for free vibration analysis of solid and thin-walled structures. *Journal of Sound and Vibration*, 332(23):6104-6127. https://doi.org/10.1016/j.jsv.2013.06.023

Pagani A, Petrolo M, Colonna G, et al., 2015. Dynamic response of aerospace structures by means of refined beam theories. *Aerospace Science and Technology*, 46:360-373. https://doi.org/10.1016/j.ast.2015.08.005

Pagani A, de Miguel AG, Petrolo M, et al., 2016. Analysis of laminated beams via Unified Formulation and Legendre polynomial expansions. *Composite Structures*, 156:78-92. https://doi.org/10.1016/j.compstruct.2016.01.095

Stephen NG, Levinson M, 1979. A second order beam theory. *Journal of Sound and Vibration*, 67(3):293-305. https://doi.org/10.1016/0022-460X(79)90537-6

Tetsuo I, 1990. Timoshenko beam theory with extension effect and its stiffness equation for finite rotation. *Computers & Structures*, 34(2):239-250. https://doi.org/10.1016/0045-7949(90)90367-B

Timoshenko SP, 1921. LXVI. On the correction for shear of the differential equation for transverse vibrations of prismatic bars. *The London*, *Edinburgh*, *and Dublin Philosophical Magazine and Journal of Science*, 41(245):744-746. https://doi.org/10.1080/14786442108636264

Timoshenko SP, 1922. X. On the transverse vibrations of bars of uniform cross-section. *The London*, *Edinburgh*, *and Dublin Philosophical Magazine and Journal of Science*, 43(253):125-131. https://doi.org/10.1080/14786442208633855

Vo TP, Thai HT, 2012. Static behavior of composite beams using various refined shear deformation theories. *Composite Structures*, 94(8):2513-2522. https://doi.org/10.1016/j.compstruct.2012.02.010

中文概要

题　目：基于一维高阶理论的矿井提升机阶梯主轴静力分析

目　的：研究基于 Carrera 通用表达式的一维高阶理论，将其应用于矿井提升机主轴的力学特性分析，针对矿井提升的特殊工况对主轴模型进行改进，并探究该改进模型在工况监测中的可用性。

创新点：基于 Carrera 一维高阶理论，建立提升机主轴的一维高阶模型；根据矿井提升的特殊工况对主轴模型进行改进，得到改进的主轴一维高阶模型。

方　法：1. 引入基于 Carrera 通用表达式的一维高阶理论，克服传统梁理论的局限性和三维有限元法计算经济性差等问题；2. 通过理论计算、软件仿真和现场试验（图 14 和 15），验证改进的主轴一维高阶模型的有效性和可用性。

结　论：1. 基于 Carrera 通用表达式的一维高阶理论模型能够以较少的计算量得出与 ANSYS 三维实体模型相近的结果；2. 改进的提升机主轴一维高阶模型能够准确地监测矿井提升系统的工况。

关键词：Carrera 通用表达式；一维高阶理论；有限元法；应变场；阶梯主轴